Available online at www.sciencedirect.com
SCIENCE DIRECT®
Journal of Computational Physics 213 (2006) 659–675
JOURNAL OF COMPUTATIONAL PHYSICS
www.elsevier.com/locate/jcp

Improving Godunov-type reconstructions for simulation of vortex-dominated flows

Lei Tang [a,*], James D. Baeder [b]

[a] ZONA Technology, Inc., 9489 E. Ironwood Square Dr., Suite 100, Scottsdale, AZ 85251, USA
[b] Department of Aerospace Engineering, University of Maryland, College Park, MD 20742, USA

Received 26 September 2004; received in revised form 13 July 2005; accepted 30 August 2005
Available online 7 October 2005

Abstract

A systematic Fourier accuracy analysis is performed to examine the numerical diffusion inherent in a Godunov-type reconstruction, including both the reconstruction of the solution within each cell and the computation of the derivative terms of the reconstruction. It is found that compared with the more popular fifth-order polynomial fit of the interface values, a piecewise quadratic reconstruction of the solution with more accurate slope and curvature, especially those computed by compact difference schemes, is much less dissipative. Therefore, further given in the paper is a general framework to make a piecewise quadratic reconstruction free of numerical oscillations around the shocks. The improved accuracy and robustness of the resulting Godunov-type schemes for simulation of vortex-dominated flows are demonstrated with the numerical results of several carefully selected cases, including vortex convection and shock–vortex interaction.

Keywords: Godunov-type schemes; Piecewise quadratic reconstruction; Compact differences; Monotone schemes; Vortex-dominated flows

1. Introduction

Compared with full-potential methods, Euler/Navier–Stokes analyses include two extra physical mechanisms. They are theoretically able to correctly capture strong shocks and convect vorticity. However, this is not necessarily true for their numerical solutions. On the one hand, great progress has been made in the computational fluid dynamics (CFD) community to correctly capture strong shocks numerically. As a result, the application of Euler/Navier–Stokes analyses in the fixed-wing industry has become relatively mature. Among those so-called shock-capturing schemes, Godunov-type schemes are more popular due to their robustness. On the other hand, because of large numerical diffusion contained in such upwind schemes and insufficient grid resolution in the vortex region, it is a common experience that the predicted vortex structure is diffused very rapidly as the vortex is convected in the flowfield (e.g. [1–3]). This situation as well as high computational

* Corresponding author. Tel.: +1 4809459988; fax: +1 4809456588.
E-mail addresses: tangl@zonatech.com (L. Tang), baeder@eng.umd.edu (J.D. Baeder).

0021-9991/$ - see front matter
doi:10.1016/j.jcp.2005.08.030

intensity have severely hampered the widespread application of Euler/Navier–Stokes analyses in the rotary-wing industry.

Accurate Euler/Navier–Stokes simulation of rotary-wing aerodynamics and acoustics is much more challenging than its fixed-wing counterpart. This is because the strong tip vortices trailing from the blades stay close to the rotor disk, and thereby effectively change the angles of attack of the blades and the blade loading by producing a complicated three-dimensional-induced velocity field there. In a low-speed descending forward flight, it is even possible for these tip vortices to generate strong interactions with the rotor blades, resulting in vibration and BVI (Blade–Vortex Interaction) noise. As a result, a rotary-wing Euler/Navier–Stokes solver is required to not only correctly capture strong shocks but also accurately preserve the tip vortex structure. The accuracy deficiency of current rotor Euler/Navier–Stokes codes for vortex preservation has led previous rotor Euler/Navier–Stokes researches to focus on coupling Euler/Navier–Stokes solutions with a separate wake model by the surface transpiration (e.g. [4–7]), field velocity (e.g. [8]), or perturbation (e.g., [9]) methods. Therefore, the advantages of Euler/Navier–Stokes analyses are not fully utilized.

There are several approaches for improving the accuracy of Euler/Navier–Stokes analyses: *h*(mesh size)-, *p*(the order of the interpolant)-, *hp*-, and *r*(mesh redistribution)-refinement. *h*-methods improve the accuracy by mesh refinement with a fixed, usually low-order, interpolant, *p*-methods by increasing the order of the interpolant with a fixed mesh size, *hp*-methods by combining *h*- and *p*-refinement, and *r*-methods by mesh movement. Traditionally, finite difference schemes are designed for *h*-refinement, where the order of accuracy, i.e., the order of truncation errors, plays a key role, representing the convergence rate of the numerical solutions with mesh refinement. However, *h*-refinement is not suitable for some applications like direct numerical simulation (DNS)/large-eddy simulation (LES) of turbulence, in which the largest mesh size allowed by computer memory is usually already used. In those situations, a *p*-refinement approach is required where instead of the order of accuracy, the resolution capability of a numerical scheme becomes a more appropriate measure of accuracy [10], measured by the range of the scales which the numerical scheme can well resolve. Recently, a new family of finite difference schemes has been developed to improve the resolution capability of the traditional finite difference schemes at the cost of their order of accuracy (e.g. [10–14]). There is also a resurgence of using high-order compact differences instead of divided differences to achieve spectral-like resolution (e.g. [11,14–17]). In this paper, we will continue the above efforts and search for an effective way to improve the resolution capability of the Godunov-type schemes and thus reduce their numerical diffusion. As will be shown later, this *p*-refinement approach is more efficient than *h*-refinement approach for improving the simulation of vortex-dominated flows.

Many current Godunov-type scheme-based research and production CFD codes, e.g., *CFL3D* [18], *OVERFLOW* [19], and *TURNS* [20], follow van Leer's *MUSCL* approach [21] with a third-order polynomial fit of the interface values to compute the inviscid fluxes in the smooth regions. However, this third-order spatial discretization has been found too dissipative for simulation of vortex-dominated flows [1,3,22]. A fifth-order polynomial fit has been suggested to replace this more traditional third-order spatial discretization for better vortex preservation (e.g. [22–25]). In fact, this fifth-order polynomial fit has also been used in many monotone schemes (e.g. [26,27]) for the smooth regions to achieve higher accuracy over the *MUSCL* approach. Although large accuracy improvement has been observed with the use of this fifth-order spatial discretization (e.g. [22–25]), there is still a large room left for further accuracy improvement [28]. In order to search for a more effective approach for improvement of the resolution capability of the Godunov-type schemes and thus reduction of their numerical diffusion, a systematic Fourier accuracy analysis is performed in this paper to investigate the spectral distribution of numerical errors inherent in a Godunov-type reconstruction, including both the reconstruction of the solution within each cell and the computation of the derivative terms of the reconstruction.

The paper is organized as follows. First, the classical Fourier accuracy analysis is performed in Section 2 to investigate the numerical errors inherent in various Godunov-type reconstructions. It is found that compared with using the more popular fifth-order polynomial fit of the interface values, the use of a piecewise quadratic reconstruction of the solution with more accurate slope and curvature, especially those computed with compact differences, is much more effective for reduction of numerical diffusion. Therefore, further given in Section 3 is a general framework to make a piecewise quadratic reconstruction free of numerical oscillations. Finally, Section 4 presents the numerical results of several carefully selected cases, including both vortex

convection and shock–vortex interaction, to demonstrate the enhanced capability of the improved Godunov-type schemes for simulation of vortex-dominated flows. It is noteworthy that these improved Godunov-type schemes can also be used to improve DNS/LES of turbulence and computational acoustics.

2. Spectral analysis of reconstruction errors

Given the one-dimensional conservation law

$$u_t + f(u)_x = 0 \tag{1}$$

a Godunov-type scheme first integrates Eq. (1) over the interval $[x_{j-1/2}, x_{j+1/2}]$

$$(\bar{u}_j)_t + \frac{f(u_{j+1/2}) - f(u_{j-1/2})}{\Delta x} = 0, \tag{2}$$

with $\bar{u}_j(t) = \frac{1}{\Delta x}\int_{x_{j-1/2}}^{x_{j+1/2}} u(x,t)\,\mathrm{d}x$ and then determines the numerical fluxes at the interfaces, $f(u_{j\pm1/2})$, in two stages. The first is a projection (reconstruction) stage, in which the left/right-hand-side values of the state variables at the interfaces, $u^{\mathrm{L}}_{j\pm1/2}$ and $u^{\mathrm{R}}_{j\pm1/2}$, are computed through the interpolation of $\bar{u}_i$ $(i = j-l,\ldots,j+r)$. The second stage is an evolution (upwind) stage, in which $f(u_{j\pm1/2})$ are computed from the given $u^{\mathrm{L}}_{j\pm1/2}$ and $u^{\mathrm{R}}_{j\pm1/2}$ by locally solving a Riemann problem at the interfaces $x_{j\pm1/2}$. The focus of this paper is on the first stage. We will discuss how to effectively reduce the numerical diffusion contained in such types of upwind schemes by carefully designing a reconstruction of the solution within each cell to accurately compute $u^{\mathrm{L}}_{j\pm1/2}$ and $u^{\mathrm{R}}_{j\pm1/2}$. The classical Fourier accuracy analysis of various Godunov-type reconstructions will be performed for the linear case of $f(u) = u$.

If $u(x,t) = T(t)\,\mathrm{e}^{\mathrm{I}kx}$, where $\mathrm{I} = \sqrt{-1}$ and k is called the wave number, then

$$\bar{u}_j = \frac{\sin(\phi/2)}{\phi/2}\,\mathrm{e}^{\mathrm{I}kx_j}T(t) \tag{3}$$

and the analytical solution of $(\overline{u_x})_j$ is

$$(\overline{u_x})_j = \mathrm{I}\cdot 2\sin(\phi/2)\frac{\mathrm{e}^{\mathrm{I}kx_j}}{\Delta x}T(t), \tag{4}$$

where $\phi = k\Delta x$ is called the phase angle. On the other hand, the numerical approximation of $(\overline{u_x})_j$ given by a Godunov-type scheme is found as

$$(\overline{u_x})_j = \frac{u_{j+1/2} - u_{j-1/2}}{\Delta x} = \{A(\phi) + \mathrm{I}\cdot P(\phi)\}\frac{\mathrm{e}^{\mathrm{I}kx_j}}{\Delta x}T(t). \tag{5}$$

Therefore, the numerical dissipative (amplitude) error of the approximation is defined as

$$\varepsilon_{\mathrm{a}} = A(\phi) \tag{6}$$

and the dispersion (phase) error is defined as

$$\varepsilon_{\mathrm{p}} = P(\phi) - 2\sin(\phi/2). \tag{7}$$

2.1. Piecewise linear reconstruction

According to [29], most Godunov-type schemes use a piecewise linear reconstruction of the solution

$$\Re_j(x) = \bar{u}_j + \bar{s}_j(x - x_j) \quad (x_{j-1/2} < x < x_{j+1/2}) \tag{8}$$

and improve the accuracy of the schemes by using a higher-order polynomial interpolation to compute the cell-averaged slope $\bar{s}_j$. If the slope $\bar{s}_j$ in (8) is computed by a central divided difference scheme

$$\bar{s}_j = \frac{1}{\Delta x}\sum_l c_l(\bar{u}_{j+l} - \bar{u}_{j-l}) \tag{9}$$

then the numerical dissipative (amplitude) error of (5) is

$$\varepsilon_a = \frac{\sin(\phi/2)}{\phi/2}\left(1 - \cos\phi - \sin\phi \sum_l c_l \sin l\phi\right) \tag{10}$$

and the dispersion (phase) error is

$$\varepsilon_p = \frac{\sin(\phi/2)}{\phi/2}\left[\sin\phi + (1 - \cos\phi)\sum_l c_l \sin l\phi - \phi\right]. \tag{11}$$

Fig. 1 presents the numerical dissipative and dispersion errors of (5) based on the piecewise linear reconstruction of (8) with the second-, fourth- and sixth-order central divided difference computed slope $\bar{s}_j$, labeled as *L*2*d*, *L*4*d* and *L*6*d*, respectively. Here *L* stands for a piecewise *L*inear reconstruction, and 2*d*, 4*d*, and 6*d* represent second-, fourth- and sixth-order *d*ivided differences, respectively. It is found that all three reconstructions produce positive amplitude error (numerical damping) in the whole frequency domain, increasing with the frequency of a solution except near the high-frequency end. The use of a fourth-order divided difference instead of a second-order one to compute the slope of the reconstruction can slightly reduce the initial increment of numerical diffusion with frequency and the further accuracy improvement of the computed slope from fourth-order to sixth-order produces even much smaller reduction of numerical diffusion. Moreover, using a higher-order accurate slope is found to produce larger positive (leading) phase error in the median-frequency range but smaller negative (lag) phase error in the high-frequency range. Globally speaking, the accuracy of the three reconstructions are in the same level and severely limited by the piecewise linear reconstruction of (8).

2.2. Piecewise quadratic reconstruction

Let us further consider a piecewise quadratic reconstruction

$$\Re_j(x) = \bar{u}_j + \bar{s}_j(x - x_j) + \frac{\bar{\sigma}_j}{2}\left\{(x - x_j)^2 - \frac{\Delta x^2}{12}\right\} \quad (x_{j-1/2} < x < x_{j+1/2}). \tag{12}$$

Here $\bar{s}_j$ and $\bar{\sigma}_j$ are the cell-averaged values of the slope and curvature at x_j, respectively. By taking the same Fourier accuracy analysis as the one for a piecewise linear reconstruction, the numerical dissipative error of (5) is found as

$$\varepsilon_a = \frac{\sin(\phi/2)}{\phi/2}\left\{\left[1 + \sum_l \frac{d_l}{6}(\cos l\phi - 1)\right](1 - \cos\phi) - \sin\phi \sum_l c_l \sin l\phi\right\} \tag{13}$$

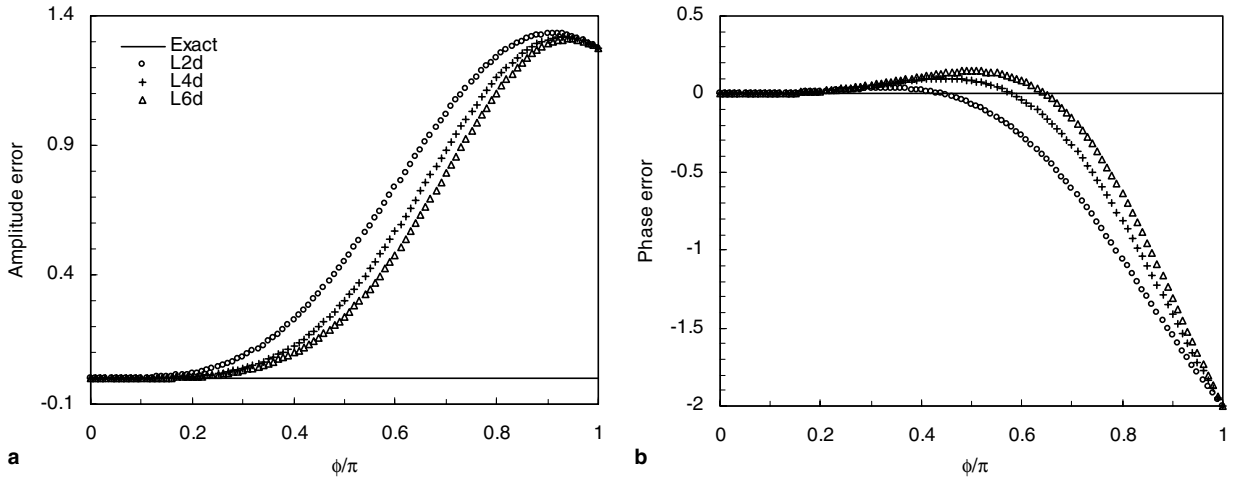

Fig. 1. Dissipative and dispersion errors of piecewise linear reconstructions. (a) Dissipation error. (b) Dispersion error.

and the dispersion error as

$$\varepsilon_p = \frac{\sin(\phi/2)}{\phi/2}\left\{\left[1+\sum_l \frac{d_l}{6}(\cos l\phi - 1)\right]\sin\phi + (1-\cos\phi)\sum_l c_l \sin l\phi - \phi\right\} \tag{14}$$

if $\bar{s}_j$ is computed by the central divided difference scheme of (9) and $\bar{\sigma}_j$ is by

$$\bar{\sigma}_j = \frac{1}{\Delta x^2}\sum_l d_l(\bar{u}_{j+l} - 2\bar{u}_j + \bar{u}_{j-l}). \tag{15}$$

Presented in Fig. 2 are the numerical dissipative and dispersion errors of (5) based on the piecewise quadratic reconstruction of (12) with the second-, fourth-, and sixth-order central divided difference computed $\bar{s}_j$ and $\bar{\sigma}_j$, labeled as $Q2d$, $Q4d$, and $Q6d$, respectively. Here Q stands for a piecewise Quadratic reconstruction. It is found that compared with using a piecewise linear reconstruction with more accurate slope, it is more effective to use a piecewise quadratic reconstruction for reduction of numerical diffusion. The accuracy improvement achieved from using more accurate derivatives for a piecewise quadratic reconstruction is also much larger than for a piecewise linear one. As shown in Fig. 2(b), the achieved reduction of numerical phase error from the use of a piecewise quadratic reconstruction is even more impressive. Different from its piecewise linear counterpart, using the higher-order accurate slope and curvature in a piecewise quadratic reconstruction reduces the numerical phase error over the whole frequency domain.

It is noteworthy that in the smooth regions, the famous piecewise-parabolic method (PPM) [30] reduces to

$$u_{j+1/2} = \tfrac{7}{12}(\bar{u}_{j+1} + \bar{u}_j) - \tfrac{1}{12}(\bar{u}_{j+2} + \bar{u}_{j-1}), \tag{16}$$

which can be derived from the piecewise quadratic reconstruction of (12) with

$$\bar{s}_j = \frac{-2\bar{u}_{j-1} - 3\bar{u}_j + 6\bar{u}_{j+1} - \bar{u}_{j+2}}{6\Delta x}, \quad \bar{\sigma}_j = \frac{\bar{u}_{j-1} - 2\bar{u}_j + \bar{u}_{j+1}}{\Delta x^2}. \tag{17}$$

It is clear that PPM is slightly different from the above other piecewise quadratic reconstructions using the central difference computed slope and curvature. As a result, in the smooth regions, whereas the above other piecewise quadratic reconstructions ultimately lead to upwind-biased discretizations of the flux derivative $(\overline{u_x})_j$, PPM produces a fourth-order central difference of the flux derivative $(\overline{u_x})_j$

$$(\overline{u_x})_j = \frac{\bar{u}_{j-2} - 8\bar{u}_{j-1} + 8\bar{u}_{j+1} - \bar{u}_{j+2}}{12\Delta x}. \tag{18}$$

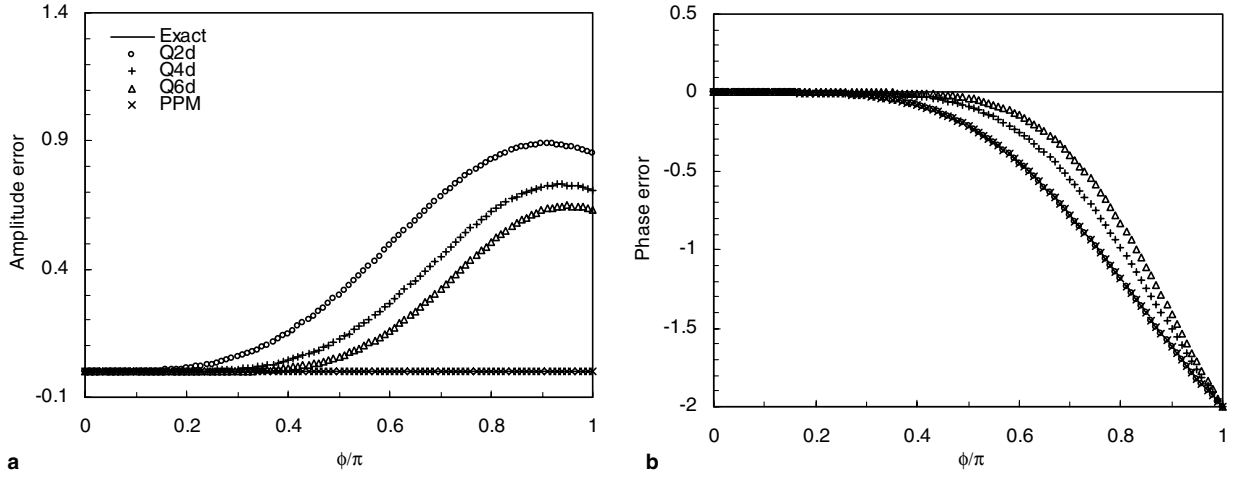

Fig. 2. Dissipative and dispersion errors of piecewise quadratic reconstructions. (a) Dissipation error. (b) Dispersion error.

Accordingly, as shown in Fig. 2(a), *PPM* has no numerical dissipation in the smooth regions. On the other hand, its numerical dispersion error, as indicated in Fig. 2(b), is same as *Q*2*d* because it only enlarges the stencil of *Q*2*d* by one.

2.3. Improvements over third-order polynomial interpolation

As mentioned earlier, many current Godunov-type scheme-based CFD codes follow van Leer's *MUSCL* approach [21] and attain their best accuracy by using a third-order polynomial fit of the interface values in the smooth regions (e.g. [18–20]). However, this third-order polynomial fit is found too dissipative for simulation of the vortex-dominated flows [1,3,22]. Therefore, a fifth-order polynomial fit has been investigated and large accuracy improvement has been observed with the use of this fifth-order spatial discretization (e.g. [22–25]).

To further explore a more effective way for accuracy improvement over the third-order polynomial fit of the interface values, we reinterpret the above third-order polynomial interpolation as a piecewise quadratic reconstruction of (12) with the second-order divided difference computed slope and curvature, i.e., *Q*2*d*. Besides using the more popular fifth-order polynomial fit, as discussed in the last section, there is another way to improve the accuracy of the computed interface values over the third-order polynomial fit or *Q*2*d*. One can keep using the piecewise quadratic reconstruction of (12) but with the more accurate slope and curvature such as *Q*4*d* and *Q*6*d*. Fig. 3 presents the numerical dissipation and dispersion errors of (5) based on the above third- and fifth-order polynomial fits of the interface values as well as several piecewise quadratic reconstructions. It is found that the accuracy improvement of *Q*4*d* over *Q*2*d* is already very close to that of the fifth-order polynomial fit over the third-order polynomial fit although those higher-order reconstruction terms of the fifth-order polynomial interpolation are not included in (12). Further use of *Q*6*d* even creates a larger accuracy improvement over the third-order polynomial fit than the fifth-order polynomial fit.

It is important to note that different from *Q*2*d*, which can also be considered as a third-order polynomial interpolation, neither *Q*4*d* nor *Q*6*d* is a polynomial interpolation but only a piecewise polynomial one. The higher accuracy of *Q*6*d* over the fifth-order polynomial fit confirms the argument in numerical analysis that a piecewise polynomial interpolation has a much better approximation property than a higher-order polynomial interpolation [31]. Using an accurate piecewise polynomial interpolation is more effective for the accuracy improvement than a higher-order polynomial interpolation. Here for clarity, a polynomial interpolation is confined to a reconstruction with the same polynomial interpolation for computing the derivatives, and an accurate piecewise polynomial interpolation is confined to a reconstruction with the derivatives much more accurate than the reconstruction itself.

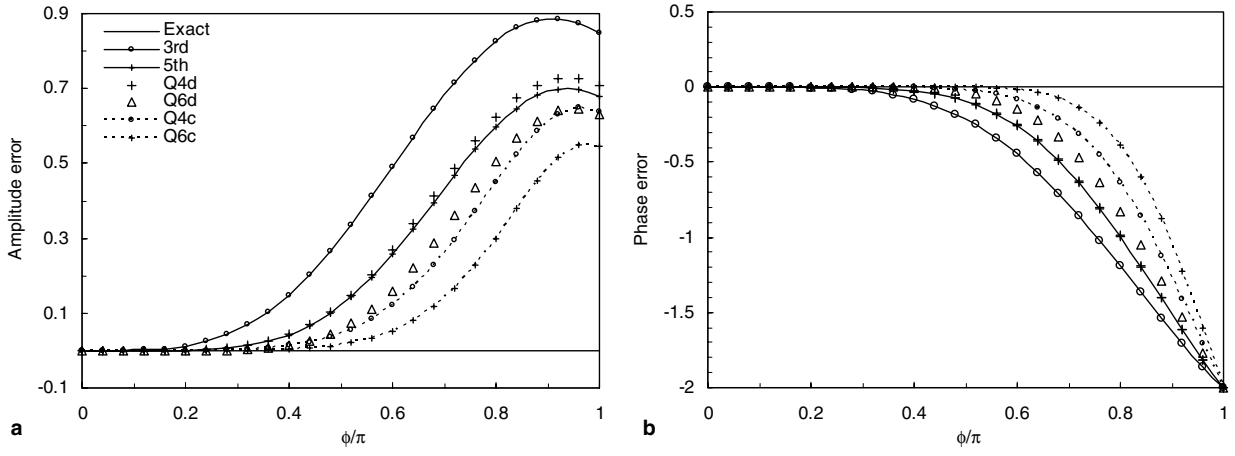

Fig. 3. Comparison of piecewise polynomial and polynomial interpolations. (a) Dissipation error. (b) Dispersion error.

However, one may argue that the higher accuracy of *Q6d* comes from its larger stencil than that of the fifth-order polynomial fit. The accuracy of *Q6d* cannot compete with that of the seventh-order polynomial fit, which uses the same stencil as *Q6d*. This is true. But remember that one does not need to use divided differences to compute the slope and curvature of a piecewise quadratic reconstruction, which are not accurate enough to make a piecewise polynomial interpolation more superior than a polynomial interpolation with the same stencil. More accurate methods such as the compact differences can be used.

Given $2l+1$ cell-averaged values of the solution around the point j, a tridiagonal central difference scheme for the approximation of the cell-averaged values of the slope can be written in the form

$$a\bar{s}_{j-1} + \bar{s}_j + a\bar{s}_{j+1} = \frac{1}{\Delta x}\sum_l c_l(\bar{u}_{j+l} - \bar{u}_{j-l}) \tag{19}$$

and for the curvature can be written in the form

$$b\bar{\sigma}_{j-1} + \bar{\sigma}_j + b\bar{\sigma}_{j+1} = \frac{1}{\Delta x^2}\sum_l d_l(\bar{u}_{j+l} - 2\bar{u}_j + \bar{u}_{j-l}). \tag{20}$$

A divided difference scheme is a special case of (19) or (20) as a or b is equal to zero. Otherwise, it is called as a compact difference scheme. If the slope $\bar{s}_j$ and the curvature $\bar{\sigma}_j$ in a piecewise quadratic reconstruction of (12) are computed by the above compact differences, then the numerical dissipation error of (5) is

$$\varepsilon_a = \frac{\sin(\phi/2)}{\phi/2}\left\{\left[1 + \sum_l \frac{d_l(\cos l\phi - 1)}{6(1+2b\cos\phi)}\right](1-\cos\phi) - \sin\phi\,\frac{\sum_l c_l \sin l\phi}{1+2a\cos\phi}\right\} \tag{21}$$

and the dispersion error is

$$\varepsilon_p = \frac{\sin(\phi/2)}{\phi/2}\left\{\left[1 + \sum_l \frac{d_l(\cos l\phi - 1)}{6(1+2b\cos\phi)}\right]\sin\phi + \frac{\sum_l c_l \sin l\phi}{1+2a\cos\phi}(1-\cos\phi) - \phi\right\}. \tag{22}$$

As shown in Fig. 3, with a smaller or equivalent stencil, the piecewise quadratic reconstruction of (12) with the fourth- or sixth-order central compact difference computed $\bar{s}_j$ and $\bar{\sigma}_j$, *Q4c* or *Q6c* with *c* standing for *c*ompact differences, has much less numerical dissipation and dispersion errors than the fifth-order polynomial fit.

3. Monotonicity-preserving piecewise quadratic reconstruction

However, it is well known that any high-order linear numerical discretization would create numerical oscillations around a discontinuity. During the last three decades, two major approaches have been developed for construction of a monotonicity-preserving high-order nonlinear scheme. One is the slope-limiting approach like flux-corrected transport (FCT) and total variation diminishing (TVD) schemes (e.g. [32–38]), and the other is essentially non-oscillatory (ENO) and weighted ENO (WENO) schemes (e.g. [13,16,17,26,39–43]). The major problem of the slope-limiting approach is the loss of accuracy at local extrema because of its TVD property. So, the approach is not suitable for simulation of vortex-dominated flows. But this situation has changed after Huynh successfully extends the slope-limiting approach beyond the TVD concept [44]. In [44], the lower and upper bounds are designed for the slope to make a piecewise linear reconstruction monotonicity-preserving. The developed monotonicity-preserving constraints are less restrictive than the TVD counterparts in that they can distinguish between a smooth local extremum and a genuine O(1) discontinuity. As a result, the accuracy of a resulting monotonicity-preserving piecewise linear reconstruction is comparable to the WENO scheme in [26]. In this approach, the enforcement of monotonicity-preserving constraints on the slope of a piecewise linear reconstruction is a post-processing step after computation of the slope. So, the extra computational cost due to implementation of monotonicity-preserving constraints for compact differences is same as that for divided differences. On the other hand, in the ENO/WENO approach, the use of compact differences for hyperbolic system of conservation laws requires a block tridiagonal matrix inversion with pivoting to implement the characteristic decomposition. The approach is computationally much more costly than its divided difference counterpart and

Huynh's approach. Moreover, the compact WENO scheme in [17] does not work for Woodward and Colella's interacting blast wave case [45], whereas in Huynh's approach, compact differences are as robust as divided differences. As shown in the above Fourier accuracy analysis, however, compared with a piecewise quadratic reconstruction, a piecewise linear reconstruction is much less effective for accuracy improvement. Therefore, in the following, we will discuss how to construct a monotonicity-preserving piecewise quadratic reconstruction using an approach similar to Huynh's work in [44].

Let us start with the construction of the upper bound of the slope. It is well known that a locally large slope is the major cause of numerical oscillations. Given a high-order polynomial interpolation, there exists an upper bound for the slope, beyond which the high-order polynomial interpolation would overshoot/undershoot the solution. The enforcement of this upper bound on the slope of the given interpolation could make the interpolation monotonicity-preserving, but at the same time produces extra numerical dissipation. The stricter the upper bound is, the larger the extra numerical dissipation introduced would be. It is known that the upper bound of the slope for a piecewise linear reconstruction is $\min(2|\Delta^+|, 2|\Delta^-|)$ (e.g., [44]), where $\Delta^+ = (\bar{u}_{j+1} - \bar{u}_j)/\Delta x$ and $\Delta^- = (\bar{u}_j - \bar{u}_{j-1})/\Delta x$. For a piecewise quadratic reconstruction, on the other hand, given monotonically increasing data, the sufficient and necessary condition of local monotonicity is

$$\begin{cases} \Re_j(x_{j-1/2}) \geqslant \bar{u}_{j-1}, \\ \Re_j(x_{j+1/2}) \leqslant \bar{u}_{j+1}, \\ \frac{d\Re_j}{dx}(x_{j-1/2}) \geqslant 0, \\ \frac{d\Re_j}{dx}(x_{j+1/2}) \geqslant 0, \end{cases} \tag{23}$$

which gives

$$\begin{cases} -12\Delta^- + 6\bar{s}_j \leqslant \bar{\sigma}_j \Delta x \leqslant 12\Delta^+ - 6\bar{s}_j, \\ -2\bar{s}_j \leqslant \bar{\sigma}_j \Delta x \leqslant 2\bar{s}_j. \end{cases} \tag{24}$$

This is valid only if

$$\begin{cases} -12\Delta^- + 6\bar{s}_j \leqslant 2\bar{s}_j, \\ -2\bar{s}_j \leqslant 12\Delta^+ - 6\bar{s}_j. \end{cases} \tag{25}$$

As a result, one yields

$$\bar{s}_j \leqslant \min(3\Delta^+, 3\Delta^-). \tag{26}$$

Similarly, for monotonically decreasing data, the sufficient and necessary condition of local monotonicity leads to $\bar{s}_j \geqslant \min(3\Delta^+, 3\Delta^-)$. In general, the upper bound of the slope for a piecewise quadratic reconstruction is $\min(3|\Delta^+|, 3|\Delta^-|)$. It is clear that a monotonicity-preserving piecewise quadratic reconstruction allows a larger upper bound for the slope than a piecewise linear one because its curvature term can partially offset the effect of a large slope. As a result, the Godunov-type scheme based on a monotonicity-preserving piecewise quadratic reconstruction is less dissipative than the one based on a monotonicity-preserving piecewise linear reconstruction in [44].

The above result seems contradictory to the common sense that considers a higher-order polynomial interpolation always unfavorable to monotonicity preservation. This is because in a high-order polynomial interpolation, as discussed in Section 2, the reconstruction $\Re_j(x)$ is equivalent to the polynomial $\wp_j(x)$ used for computing the derivatives of $\Re_j(x)$. Given a locally large slope, while increasing the order of $\Re_j(x)$ allows a larger upper bound for the slope of $\Re_j(x)$, the increase of the order of $\wp_j(x) = \Re_j(x)$ also makes the computed slope of $\Re_j(x)$ larger. Therefore, increasing the order of a polynomial interpolation has dual effects on the generation of numerical oscillations. After the enforcement of monotonicity-preserving constraints, however, a higher-order piecewise polynomial interpolation actually gives a sharper representation of a discontinuity because of its larger upper bound for the slope, as shown in Fig. 4.

In fact, Fig. 4 also illustrates the basic principle behind the following construction of a monotonicity-preserving piecewise quadratic reconstruction when the upper bound of the slope is violated.

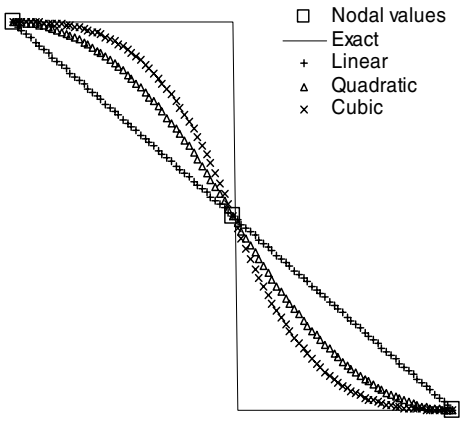

Fig. 4. Monotonicity-preserving piecewise polynomial interpolation of a discontinuity.

Theorem 3.1. *If* $|\bar{s}_j| \leqslant |\bar{s}_{j-1}|$, *then the reconstruction*

$$\Re_j(x) = \bar{u}_j + \bar{s}_j(x - x_j) + \left(-\frac{\bar{u}_j - \bar{u}_{j-1}}{\Delta x^2} + \frac{\bar{s}_j}{\Delta x}\right)\left\{(x - x_j)^2 - \frac{\Delta x^2}{12}\right\} \tag{27}$$

is locally monotonicity-preserving in the interval $[x_{j-1}, x_j]$; *otherwise the reconstruction*

$$\Re_j(x) = \bar{u}_j + \left(2\frac{\bar{u}_j - \bar{u}_{j-1}}{\Delta x} - \bar{s}_{j-1}\right)(x - x_j) + \left(\frac{\bar{u}_j - \bar{u}_{j-1}}{\Delta x^2} - \frac{\bar{s}_{j-1}}{\Delta x}\right)\left\{(x - x_j)^2 - \frac{\Delta x^2}{12}\right\} \tag{28}$$

is locally monotonicity-preserving in the interval $[x_{j-1}, x_j]$.

Proof 1. Without loss of generality, let us consider the case of increasing data only. The corresponding locally monotonicity-preserving requirement is

$$\frac{\mathrm{d}}{\mathrm{d}x}\Re_j(x) \geqslant 0. \tag{29}$$

Consider the case of $|\bar{s}_j| \leqslant |\bar{s}_{j-1}|$ first. From (27), one yields

$$\frac{\mathrm{d}}{\mathrm{d}x}\Re_j(x) = \bar{s}_j + 2\left(-\frac{\bar{u}_j - \bar{u}_{j-1}}{\Delta x^2} + \frac{\bar{s}_j}{\Delta x}\right)(x - x_j) \tag{30}$$

and from the condition of $\bar{s}_j \leqslant \bar{s}_{j-1}$, one yields

$$\frac{\bar{u}_j - \bar{u}_{j-1}}{\Delta x} - \bar{s}_j \geqslant 0. \tag{31}$$

Therefore, the reconstruction of (27) satisfies the requirement of (29) in the interval $[x_{j-1}, x_j]$. Similarly, one can prove the reconstruction of (28) is locally monotonicity-preserving in the interval $[x_{j-1}, x_j]$ if $\bar{s}_j \geqslant \bar{s}_{j-1}$. □

Based on the local conditions, this theorem provides a pair of the slope and curvature, denoted as $\bar{s}_{\mathrm{L}}$ and $\bar{\sigma}_{\mathrm{L}}$, for constructing a monotonicity-preserving piecewise quadratic reconstruction in the interval $[x_{j-1/2}, x_j]$ if $|\bar{s}_j| \geqslant 3|\Delta^-|$. The next theorem will provide their counterparts, denoted as $\bar{s}_{\mathrm{R}}$ and $\bar{\sigma}_{\mathrm{R}}$, in the interval $[x_j, x_{j+1/2}]$ for $|\bar{s}_j| \geqslant 3|\Delta^+|$.

Theorem 3.2. *If* $|\bar{s}_j| \leqslant |\bar{s}_{j+1}|$, *then the reconstruction*

$$\Re_j(x) = \bar{u}_j + \bar{s}_j(x - x_j) + \left(\frac{\bar{u}_{j+1} - \bar{u}_j}{\Delta x^2} - \frac{\bar{s}_j}{\Delta x}\right)\left\{(x - x_j)^2 - \frac{\Delta x^2}{12}\right\} \tag{32}$$

is locally monotonicity-preserving in the interval $[x_j, x_{j+1}]$; *otherwise the reconstruction*

$$\Re_j(x) = \bar{u}_j + \left(2\frac{\bar{u}_{j+1} - \bar{u}_j}{\Delta x} - \bar{s}_{j+1}\right)(x - x_j) + \left(-\frac{\bar{u}_{j+1} - \bar{u}_j}{\Delta x^2} + \frac{\bar{s}_{j+1}}{\Delta x}\right)\left\{(x - x_j)^2 - \frac{\Delta x^2}{12}\right\} \tag{33}$$

is locally monotonicity-preserving in the interval $[x_j, x_{j+1}]$.

The proof of this theorem is similar to that of Theorem 3.1.

With the above two theorems, one can enforce the upper bound of the slope for a piecewise quadratic reconstruction as follows:

$$\begin{cases} \bar{s}_L = \bar{s}_j, \bar{\sigma}_L = \bar{\sigma}_j & \text{if } |\bar{s}_j| \leqslant 3|\Delta^-|, \\ \bar{s}_L = 2\Delta^- - \bar{s}_{j-1}, \bar{\sigma}_L = 2(\Delta^- - \bar{s}_{j-1})/\Delta x & \text{if } |\bar{s}_j| > 3|\Delta^-| \end{cases} \tag{34}$$

and

$$\begin{cases} \bar{s}_R = \bar{s}_j, \bar{\sigma}_R = \bar{\sigma}_j & \text{if } |\bar{s}_j| \leqslant 3|\Delta^+|, \\ \bar{s}_R = 2\Delta^+ - \bar{s}_{j+1}, \bar{\sigma}_L = 2(-\Delta^+ + \bar{s}_{j+1})/\Delta x & \text{if } |\bar{s}_j| > 3|\Delta^+|. \end{cases} \tag{35}$$

Finally,

$$\begin{cases} \bar{s}_j = \bar{s}_L, \bar{\sigma}_j = \bar{\sigma}_L & \text{if } |\bar{s}_L| < |\bar{s}_R|, \\ \bar{s}_j = \bar{s}_R, \bar{\sigma}_j = \bar{\sigma}_R & \text{if } |\bar{s}_L| \geqslant |\bar{s}_R|. \end{cases} \tag{36}$$

It is noteworthy that different from the ENO/WENO approach, which selects the smoothest stencil near a discontinuity and does not allow the interpolation across the discontinuity, our above approach only shifts the stencil by one cell according to the local smoothness and allows the interpolation across the discontinuity. Therefore, our approach is less diffusive than the ENO/WENO approach. On the other hand, the above approach only works for the accurate $\bar{s}_j$ and $\bar{\sigma}_j$. In reality, however, as shown in [44], the slope and curvature given by finite differences in Section 2 may have the wrong sign near a discontinuity. The procedure suggested in [44] has to be used first to correct the signs of the computed slope and curvature. Furthermore, the extension of the above approach to hyperbolic systems of conservation laws requires the characteristic decomposition.

4. Numerical results and discussion

Several carefully selected cases are presented to demonstrate the improved accuracy of a Godunov-type scheme based on a piecewise quadratic reconstruction and the validity of the above monotonicity-preserving constraints for a piecewise quadratic reconstruction. The Trapezoidal scheme is chosen for time discretization although a simpler explicit scheme could be used. This is simply because there is no numerical damping in this time discretization and an implicit scheme is suitable for a larger range of problems than an explicit scheme. The implicit operator used is the lower–upper symmetric Gauss–Seidel (LU-SGS) scheme with the spectral radius approximation used in a typical rotor Euler/Navier–Stokes code, *TURNS* [20], which also has the option of using Newton-type subiterations at each time step for reduction of the linearization and factorization errors, and the improvement of time accuracy.

4.1. Woodward–Colella's two interacting blast waves

Our first selected case is Woodward–Colella's problem in [45], which involves the interaction of two blast waves. This is a much tougher case than the more popular shock-tube problems. Many schemes like the compact WENO scheme in [17] work well for the shock-tube problems but fail this case. So, we use this case here to examine the validity of the above monotonicity-preserving constraints for a piecewise quadratic reconstruction.

However, no exact solution exists for this case. The "exact" solution presented in Fig. 5 is actually the numerical solution of the *WENO5* scheme [26] on a fine mesh of 1600 points. Fig. 5(a) also presents the density distributions at $t = 0.038$ predicted by various piecewise quadratic reconstructions on a coarser mesh of 400 points with three subiterations at each time step. Here *M* in the legends stands for *M*onotonicity-preserving. It is found that the present monotonicity-preserving constraints work well for

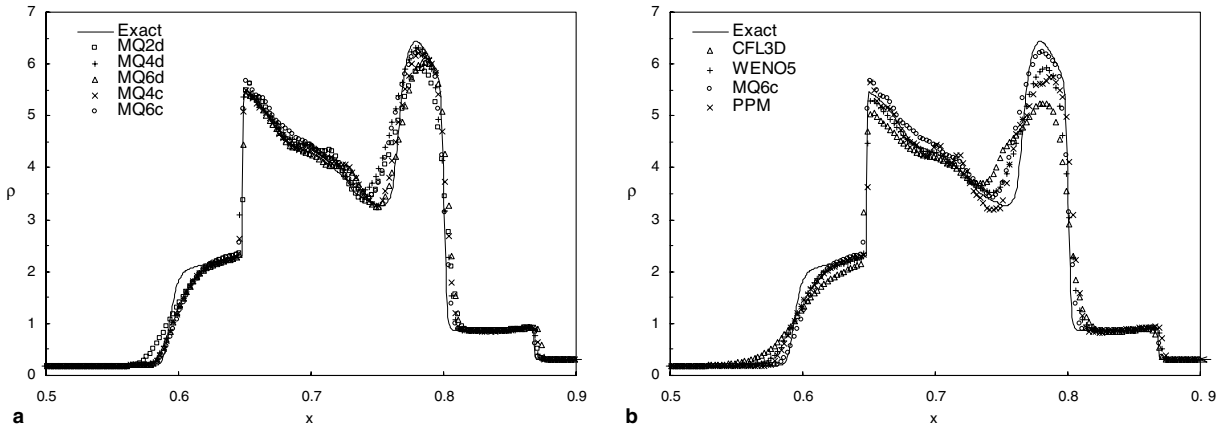

Fig. 5. Woodward–Colella's blast waves problem ($N = 400$, $\Delta t = 0.00005$, $t = 0.038$).

all piecewise quadratic reconstructions. Whereas some monotonicity-preserving piecewise quadratic reconstructions predict the value of the valley more accurately, the others give the better prediction of the right peak value. Further presented in Fig. 5(b) is the comparison of *MQ6c* with the other three more popular monotonicity-preserving reconstructions. The first two are the TVD scheme used in *CFL3D* [18] and *WENO5* in [26], which reduce to the third/fifth-order polynomial fits in the smooth regions, respectively. The third one is the more popular monotonicity-preserving piecewise quadratic reconstruction, *PPM* [30]. It is worthy to emphasize that all the computations have been performed with Roe's approximate Riemann solver and with Trapezoidal time discretization. The only difference between various computations is the different types of reconstruction used. As expected, the TVD scheme used in *CFL3D* produces the most diffusive result, whereas the result from *MQ6c* is the least diffusive.

4.2. 2-D vortex convection

This is one of our major test cases. The vortex model considered is the one due to Kauffman/Scully [46] with a core radius of $r_c = 0.05$ and the nondimensionalized strength of $\hat{\Gamma} = 0.2$. The vortex convects over a distance of $200r_c$ at a streamwise Mach number of 0.5. A small $\Delta t = 0.008333$ with four subiterations is used to maintain the time accuracy, for which the vortex convects a distance of Δx in six steps on a coarse mesh with only four points across the vortex core. The uniform Cartesian mesh has a total of 481×81 points. In this case, the perturbation induced by the vortex is not large enough to produce a significantly nonlinear effect. So, the convection is linear and the solutions should remain unchanged by convection. Any diffusion of the computed vortex is considered from the numerical discretization. Because the peak values of the vortex-induced vertical velocity are of most concern in practice, their decay due to numerical discretization will be used in the following as a basic measure to examine the numerical diffusion of vorticity inherent in various Godunov-type reconstructions.

Fig. 6 presents the decay of the normalized peak-to-peak vertical-induced velocity $\Delta v/\Delta v_0$ with respect to the number of core radii travelled predicted by the Godunov-type schemes based on several piecewise quadratic reconstructions. It is found that with only four points across the vortex core, the use of *Q*4*d*, *Q*4*c*, and *Q*6*c* reduces the decay of $\Delta v/\Delta v_0$ after 200 core radii convection predicted by *Q*2*d*, *Q*4*d*, and *Q*4*c* by at least 50%, respectively. On the other hand, *Q*6*d* and *Q*4*c* produce very similar results. Our monotonicity-preserving constraints slightly degrade the accuracy of *Q*2*d* but introduce larger extra numerical dissipation into those more accurate piecewise quadratic reconstructions. Whereas the reduction of the numerical diffusion of vorticity achieved by *MQ4d* over *MQ2d* is nearly 20% for a 200 core radii convection, the further reduction given by *MQ6d* or *MQ4c* over *MQ4d* is just around 2.5%. The difference between the results of *MQ6c* and *MQ6d* is even smaller, only 0.77% further reduction whereas *Q*6*c* is able to reduce the numerical diffusion of vorticity given by *Q*6*d* after 200 core radii convection from about 8% to 4%.

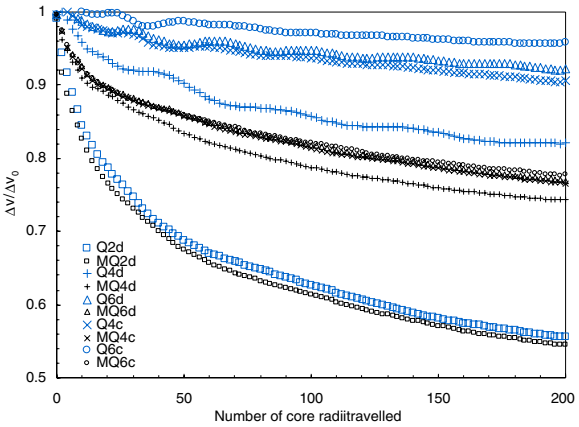

Fig. 6. Numerical vortex decay predicted by piecewise quadratic reconstructions.

Further presented in Fig. 7 is the decay of the normalized peak-to-peak vertical induced velocity predicted by *CFL3D*, *WENO5*, *MQ6c*, and *PPM*, and their equivalent viscous decay of the Lamb–Oseen vortex [47]. (The derivation of the viscous decay of the induced velocity versus the number of core radii travelled is referred to [28].) It is found that the numerical decay produced by *CFL3D* after 200 core radii convection is equivalent to the viscous decay of the Lamb–Oseen vortex at $Re \cong 507$ with the vortex core radius as the characteristic length. If the Reynolds number of a viscous flow is higher than 507, then the accuracy of *CFL3D* is unacceptable and a more accurate scheme or/and a finer mesh are needed. The use of *WENO5*, *MQ6c*, and *PPM* can raise such a critical Reynolds number to 2909, 12,261, and 3094, respectively. Based on the airfoil chord if the vortex core radius is 5% of the airfoil chord, these critical Reynolds numbers are equivalent to 10^4, 5.8×10^4, 2.45×10^5, and 6.2×10^4, respectively. It is interesting to find that *PPM* has slightly less numerical diffusion for this vortex convection case than the more advanced *WENO5*. This is because *PPM* reduces to a fourth-order central scheme in the smooth region.

The predicted vertical-induced velocity profiles after 200 core radii convection are further shown in Fig. 8. No numerical oscillation is found in these profiles. As expected, the peak value of the vertical-induced velocity profile predicted by *CFL3D* is significantly underpredicted and the predicted vortex core is diffused from 4 points to 16 points. On the other hand, *WENO5*, *MQ6c*, and *PPM* yield a profile much closer to the exact solution. *WENO5* and *PPM* double the vortex core size after 200 core radii convection and *MQ6c* only slightly increases the vortex core from 4 points to 6 points.

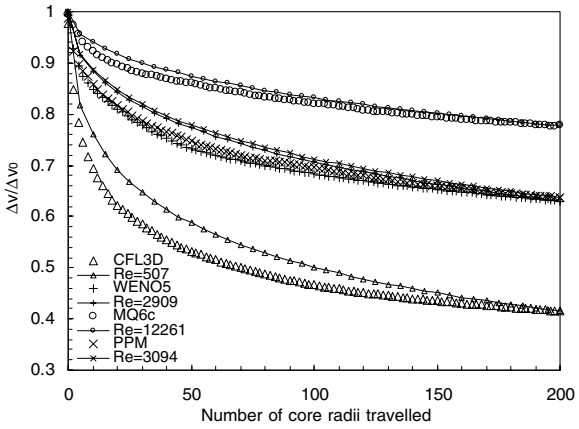

Fig. 7. Analogy of numerical decay of four monotone schemes to viscous decay.

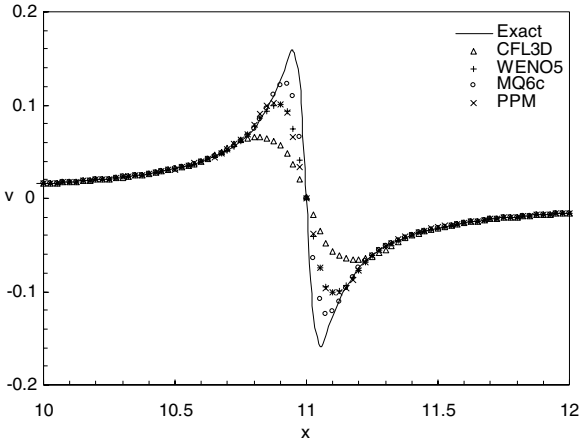

Fig. 8. Vertical-induced velocity profiles after 200 core radii convection.

Finally, Fig. 9 indicates that to achieve the accuracy of *WENO5* and *MQ6c* for this vortex convection case, *CFL3D* requires doubling and quadrupling the number of grid points, respectively. This would increase the computational cost by $2^3 = 8$ and $4^3 = 64$ times if the *CFL* number is fixed. On the other hand, *WENO5* and *MQ6c* only double the computational cost of *CFL3D*. So, a *p*-refinement approach is much more efficient than a *h*-refinement approach for improving the simulation of vortex-dominated flows.

4.3. Shock–vortex interaction

Our last case is a shock–vortex interaction case, in which a Kauffman/Scully vortex with a core radius of $r_c = 0.1$ and the nondimensionalized strength of $\hat{\Gamma} = 0.5$ is imposed on the flowfield of Yee et al.'s shock reflection problem [48]. With only four points across the vortex core, the uniform Cartesian mesh needs 241 points in the *x*-direction to cover the same convection length as the last case. Moreover, in order to achieve the same fineness ratio of the computational domain as the one in [48], 61 points are used in the *y*-direction.

The computation starts with the calculation of the steady solution of Yee et al.'s shock reflection problem [48]. In these steady computations, the first-order implicit time discretization is used with a *CFL* number of 5 and one Newton subiteration. The predicted density contours and the pressure coefficient distributions at $y = 1.5$ after 300 iterations are presented in Fig. 10. It is found that the same as *CFL3D* and *WENO5*, *MQ6c* is also able to produce clean shock profiles. On the other hand, *PPM* still causes

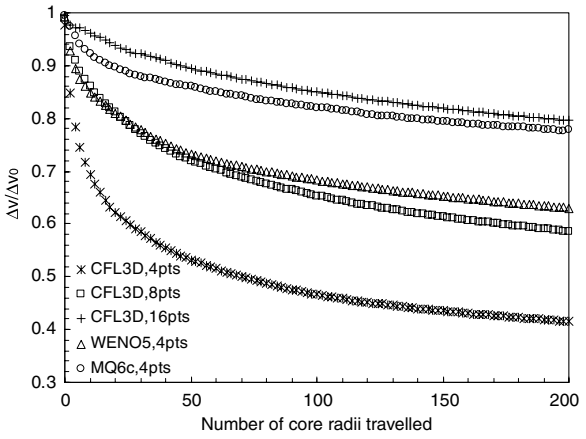

Fig. 9. *h*-refinement versus *p*-refinement.

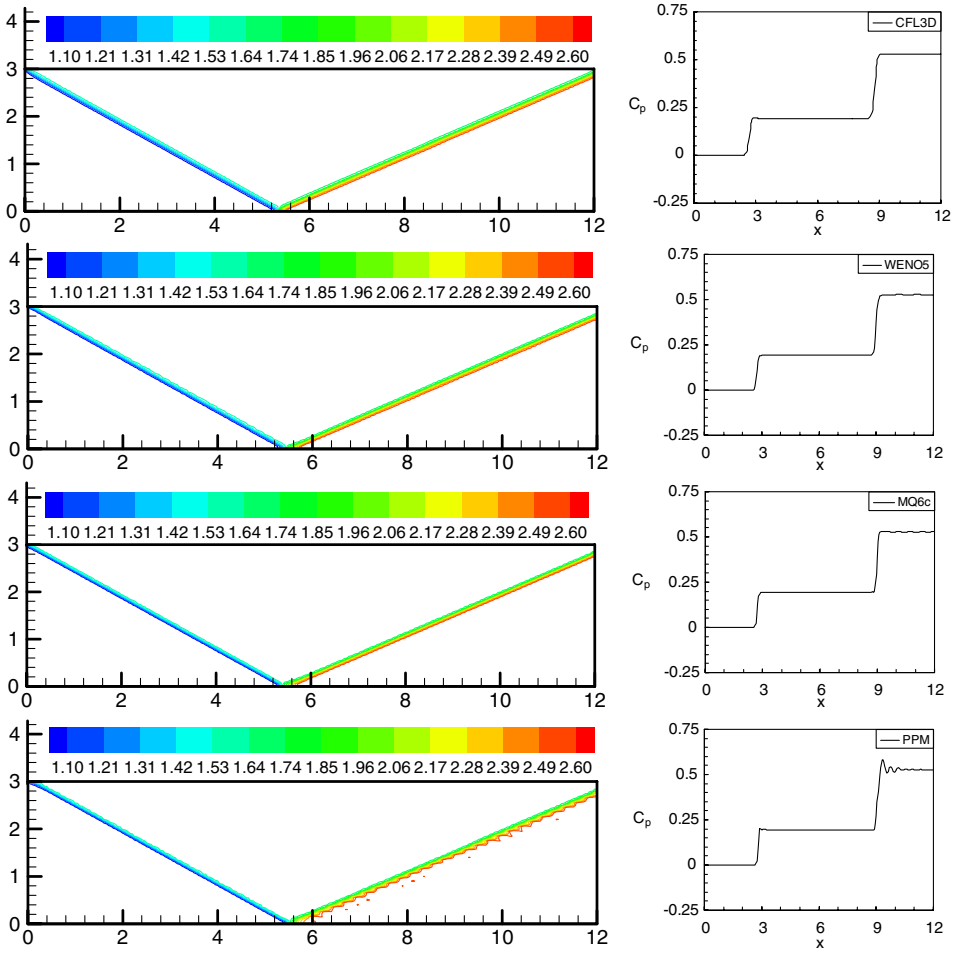

Fig. 10. Density contours and pressure coefficient distributions of Yee et al.'s shock reflection problem.

some numerical oscillations after the reflected shock. This is probably because the characteristic decomposition has only been applied to *WENO5* and *MQ6c*, whereas *CFL3D* and *PPM* work on the primitive variables.

After obtaining the above steady solutions, the vortex with $r_c = 0.1$ and $\hat{\Gamma} = 0.5$ is imposed on the flowfield at $(x, y) = (1, 1.5)$ and subsequently convects in the flowfield. In these unsteady computations, we use the Trapezoidal scheme with $\Delta t = 0.008333$, the same as the last case, but with six instead of four Newton subiterations to achieve more clean solutions. Fig. 11 presents the predicted density contours and the pressure coefficient distributions across the vortex center at the initial time step and when the vortex starts to leave the computational domain. It is found that starting with the same vortex structure at the initial time step, the vortex structure given by *CFL3D* at the later time step is the most diffused, which can be clearly seen in both the predicted density contours and the pressure coefficient distributions across the vortex center. On the other hand, *WENO5*, *MQ6c*, and *PPM* produce similar density contours. From the predicted pressure coefficient distributions across the vortex center, however, one is still able to find that *MQ6c* preserves the vortex structure better than *WENO5* and *PPM*.

It is noteworthy that since *CFL3D* and *PPM* work on the primitive variables, they are computationally more efficient. For the above steady case, *CFL3D* and *PPM* take about 19.2 and 31.7 s, respectively, on a 2.4 GHz PC. On the other hand, *WENO5* and *MQ6c* need about 40.1 and 42.5 s, respectively, for the same case on the same machine.

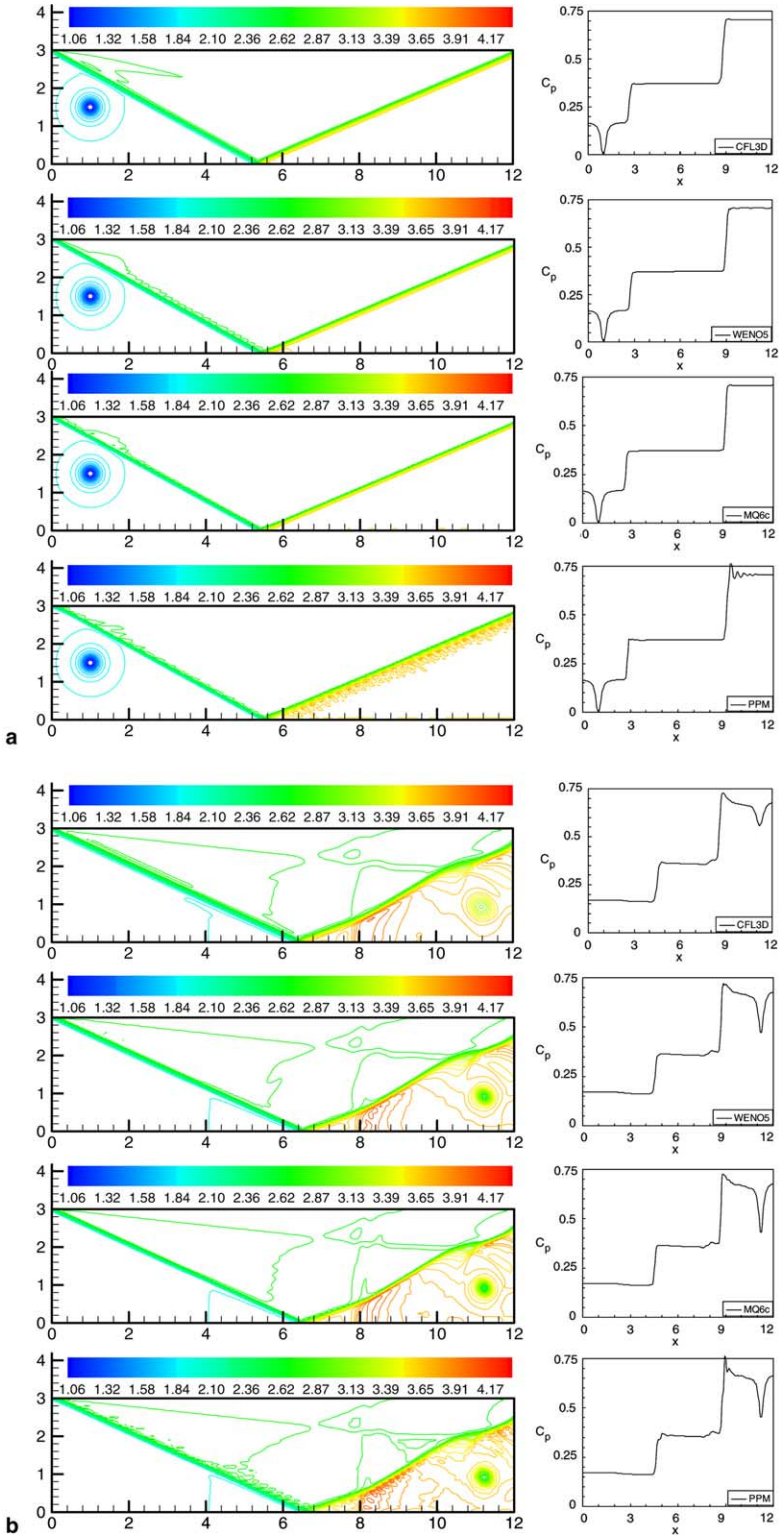

Fig. 11. Density contours and pressure coefficient distributions of shock–vortex interaction. (a) Initial time step: $t = 0$. (b) Vortex starts to leave the domain: $t = 3.83$.

5. Conclusions

Given the more traditional third-order polynomial fit of the interface values (i.e., a piecewise quadratic reconstruction with the second-order divided difference computed slope and curvature) as the baseline Godunov-type reconstruction, it is much more effective to use an improved third-order Godunov-type reconstruction, i.e., the same piecewise quadratic reconstruction form but with the more accurate sixth-order compact difference computed slope and curvature, than the more popular fifth-order polynomial fit of the interface values for reduction of numerical diffusion. A general framework has also been developed to make such a piecewise quadratic reconstruction free of numerical oscillations. The resulting improved third-order monotonicity-preserving scheme has less numerical dissipation than the more popular *PPM* and *WENO5* schemes.

Acknowledgments

This work was initiated as the first author's Ph.D. thesis work, which was partially supported by the National Rotorcraft Technology Center (NRTC) under the Rotorcraft Center of Excellence program. However, the majority of this work was done later under the support of NSF Grant DMI-0232255 to the first author.

References

[1] A.J. Landgrebe, New directions in rotorcraft computational aerodynamics research in the US, in: The 75th AGARD Fluid Dynamics Panel Meeting and Symposium on Aerodynamics and Aeroacoustics of Rotorcraft, Paper No. 1, Berlin, Germany, 1994.
[2] A.T. Conlisk, Modern helicopter aerodynamics, Ann. Rev. Fluid Mech. 29 (1997) 515.
[3] B.E. Wake, J.D. Baeder, Evaluation of a Navier–Stokes analysis method for hover performance prediction, J. Am. Helicopter Soc. 41 (1996) 7.
[4] N.L. Sankar, B.E. Wake, S.G. Lekoudis, Solution of the unsteady Euler equations for fixed and rotor wing configurations, J. Aircraft 23 (1986) 283.
[5] R.K. Agarwal, J.E. Deese, Euler calculations for flowfield of a helicopter rotor in hover, J. Aircraft 24 (1987) 231.
[6] G.R. Srinivasan, W.J. McCroskey, Navier–Stokes calculations of hovering rotor flowfields, J. Aircraft 25 (1988) 865.
[7] B.E. Wake, N.L. Sankar, Solutions of the Navier–Stokes equations for the flow about a rotor blade, J. Am. Helicopter Soc. 34 (1989) 13.
[8] H. Khanna, J.D. Baeder, Coupled free-wake/CFD solutions for rotors in hover using a field velocity approach, in: Proceedings of the American Helicopter Society 52nd Annual Forum, Washington, DC, 1996.
[9] G.R. Srinivasan, W.J. McCroskey, J.D. Baeder, Aerodynamics of two-dimensional blade–vortex interaction, AIAA J. 24 (1986) 1569.
[10] L. Tang, J.D. Baeder, Uniformly accurate finite difference schemes for *p*-refinement, SIAM J. Sci. Comput. 20 (1999) 1115.
[11] S.K. Lele, Compact finite difference schemes with spectral-like resolution, J. Comput. Phys. 103 (1992) 16.
[12] C.K.W. Tam, J.C. Webb, Dispersion-relation-preserving finite difference schemes for computational acoustics, J. Comput. Phys. 107 (1993) 262.
[13] V.G. Weirs, G.V. Candler, Optimization of weighted ENO schemes for DNS of compressible turbulence, AIAA paper 97 (1997) 1940.
[14] L. Tang, J.D. Baeder, Mixed compact schemes for high-frequency solutions, AIAA paper 97 (1997) 2093.
[15] M.R. Visbal, D.V. Gaitonde, High-order-accurate methods for complex unsteady subsonic flows, AIAA J. 37 (1999) 1231.
[16] S. Pirozzoli, Conservative hybrid compact-WENO schemes for shock–turbulence interaction, J. Comput. Phys. 178 (2002) 81.
[17] L. Jiang, H. Shan, C.Q. Liu, Weighted compact scheme for shock capturing, Int. J. Comput. Fluid Dynamics 15 (2001) 147.
[18] S.L. Krist, R.T. Biedron, C.L. Rumsey, CFL3D user's manual (version 5.0), NASA Langley Research Center 1997.
[19] P.G. Buning, D.C. Jespersen, T.H. Pulliam, G.H. Klopfer, W.M. Chan, J.P. Slotnick, S.E. Krist, K.J. Renze, OVERFLOW user's manual (version 1.8r), NASA Ames Research Center, 2000.
[20] G.R. Srinivasan, J.D. Baeder, S. Obayashi, W.J. McCroskey, Flowfield of a lifting rotor in hover – a Navier–Stokes simulation, AIAA J. 30 (1992) 2371.
[21] B. van Leer, Towards the ultimate conservative difference scheme. V. A second order sequel to Godunov's method, J. Comput. Phys. 32 (1979) 101.
[22] B.E. Wake, D. Choi, Investigation of high-order upwinded differencing for vortex convection, AIAA Paper 95 (1995) 1719.
[23] M.M. Rai, Navier–Stokes simulation of blade–vortex interaction using high-order accurate upwind schemes, AIAA paper 87 (1987) 0543.
[24] F. Davoudzadeh, H. McDonald, B.E. Thompson, Accuracy evaluation of unsteady CFD numerical schemes by vortex preservation, Comput. Fluids 24 (1995) 883.
[25] N. Hariharan, L.N. Sankar, Higher order numerical simulation of rotor flow field, in: Proceedings of the American Helicopter Society 50th Annual Forum, Washington, DC, 1994.
[26] G.-S. Jiang, C.-W. Shu, Efficient implementation of weighted ENO schemes, J. Comput. Phys. 126 (1996) 202.
[27] A. Suresh, H.T. Huynh, Accurate monotonicity preserving scheme with Runge–Kutta time-stepping, J. Comput. Phys. 136 (1997) 83.

[28] L. Tang, Improved Euler simulation of helicopter vortical flows, Ph.D. thesis, University of Maryland, College Park, 1998.
[29] H.Q. Yang, A.J. Przekwas, Unified high-order Godunov-type schemes for hyperbolic conservation laws, AIAA Paper 91 (1991) 0634.
[30] P. Colella, P. Woodward, The Piecewise Parabolic Method (PPM) for gas-dynamical simulations, J. Comput. Phys. 54 (1984) 174.
[31] C. de Boor, A Practical Guide to Splines, Springer, Berlin, New York, 1978.
[32] J.P. Boris, D.L. Book, Flux corrected transport, I SHASTA, a fluid transport algorithm that works, J. Comput. Phys. 11 (1973) 38.
[33] D.L. Book, J.P. Boris, K. Hain, Flux-corrected transport II: generalizations of the method, J. Comput. Phys. 18 (1975) 248.
[34] S.T. Zalesak, Fully multidimensional flux-corrected transport algorithms for fluids, J. Comput. Phys. 31 (1979) 335.
[35] A. Harten, On a class of high resolution total-variation-stable finite-difference schemes, SIAM J. Numer. Anal. 21 (1984) 1.
[36] P.L. Roe, Some contributions to the modeling of discontinuous flows, Lect. Appl. Math. 22 (1985) 163.
[37] P.K. Sweby, High resolution schemes using flux limiters for hyperbolic conservation laws, SIAM J. Numer. Anal. 21 (1984) 995.
[38] S.R. Chakravarthy, S. Osher, High resolution applications of the Osher upwind scheme for the Euler equations, AIAA paper 83 (1983) 1943.
[39] A. Harten, B. Engquist, S. Osher, S.R. Chakravarthy, Uniformly high order accurate essentially non-oscillatory schemes, III., J. Comput. Phys. 71 (1987) 231.
[40] C.-W. Shu, S. Osher, Efficient implementation of essentially non-oscillatory shock capturing schemes, J. Comput. Phys. 77 (1988) 439.
[41] C.-W. Shu, S. Osher, Efficient implementation of essentially non-oscillatory shock capturing schemes, II., J. Comput. Phys. 83 (1989) 32.
[42] X.-D. Liu, S. Osher, T. Chan, Weighted essentially non-oscillatory schemes, J. Comput. Phys. 115 (1994) 200.
[43] D.S. Balsara, C.-W. Shu, Monotonicity preserving weighted essentially non-oscillatory schemes with increasingly high order of accuracy, J. Comput. Phys. 160 (2000) 405.
[44] H.T. Huynh, Accurate upwind methods for the Euler equations, SIAM J. Numer. Anal. 32 (1995) 1565.
[45] P. Woodward, P. Colella, The numerical simulation of two-dimensional fluid flow with strong shocks, J. Comput. Phys. 54 (1984) 115.
[46] G.H. Vatistas, V. Kozel, W.C. Mih, A simpler model for concentrated vortices, Exp. Fluids 11 (1991) 73.
[47] S.H. Lamb, Hydrodynamics, Cambridge University Press, 1957.
[48] H.C. Yee, R.F. Warming, A. Harten, Implicit total variation diminishing (TVD) schemes for steady-state calculations, AIAA paper 83 (1983) 1902.